Simulated annealing algorithm for vascular optimization applied to the cerebral arteries

Jonathan Keelan,[1] Emma M.L. Chung,[2,3] and James P. Hague[1,*]

[1] *School of Physical Sciences, The Open University, MK7 6AA*
[2] *Cerebral Haemodynamics in Ageing and Stroke Medicine (CHiASM) group, Department of Cardiovascular Sciences, University of Leicester, LE1 7RH*
[3] *Medical Physics, University Hospitals of Leicester NHS Trust, Leicester Royal Infirmary, LE1 5WW*

Computerized models of the cerebral vasculature are becoming increasingly used for analysis of medical images, patient treatment planning and cerebral haemodynamics simulations. Previously, we presented a method based on universal physical and physiological principles for the growth of realistic cardiac vascular trees *in-silico* using simulated annealing (SA). SA was found to be capable of reliably identifying the optimal arrangement of arteries to supply the heart. In this paper, we extract volumes representing the gray and white matter of the brain from Magnetic Resonance Imaging (MRI) data and automatically generate the optimal cerebral arterial tree using simulated annealing. The cerebral arteries are arguably the most difficult to reproduce from first principles, featuring multiple substrates and interwoven territories, with a complicated layered topology. Comparison of our simulations with human angiography data confirms that vascular trees generated by our algorithm are a good match to real cerebral arteries.

I. INTRODUCTION

The brain comprises approximately 1.25 kg of fragile spongy tissue perfused by myriad branching vessels [1, 2]. Although the mass of the brain represents only two percent of body weight, it has an exceptionally high demand for oxygenated blood. Supply of blood to the brain accounts for 20% of the body's energy requirements, 14% of blood flow, and it holds approximately 700 ml of blood at any given time [3]. This exceptional thirst for blood is due to the high metabolic demand of the brain's active gray matter cells, which are contained in a 2-4 mm thick outer layer of brain tissue known as the cerebral cortex. Gray matter within the cerebral cortex requires blood at approximately double the rate of white matter [4, 5]. The requirement for a constant supply of blood to every part of the brain has resulted in the development of an exquisitely intertwined network of arteries and veins; collectively known as the cerebral vasculature. In this study we explore the extent to which the architecture of the cerebral arterial vasculature can be explained based purely on principles of fluid dynamical optimization. A computer model of the arterial blood supply to the brain is presented, developed by minimizing the energy costs associated with fluid transport *in-silico* to deduce an optimal configuration of arteries.

Major arteries supplying the brain emerge from a ring-like arrangement of arteries positioned at the base of the brain, known as the Circle of Willis (CoW). The major cerebral arteries (Anterior, Middle, and Posterior Cerebral Arteries - ACA, MCA and PCA, respectively) then penetrate the brain parenchyma (the functional part of the tissue) and branch further to supply the anterior, middle and posterior perfusion territories, before emerging at the surface (pia) of the brain and covering the cerebral cortex (a description of the cerebral vasculature can be found in e.g. Ref. [1]). The cerebral cortex features deep folds across its surface, upon which the pial arteries attach via perforating arteries to perfuse the gray matter beneath [6]. As the brain blood supply throughout the tree branches further into arterioles and tiny capillaries, the area of the vascular bed increases, causing the blood to slow almost to a standstill, thus facilitating diffusion of oxygen and nutrients through the capillary wall. Since oxygen diffuses slowly and is metabolized rapidly, brain cells need to be within easy reach (25 microns) of the nearest capillary [7].

In this study we describe *in-silico* growth of the arterial cerebral circulation starting at the major cerebral arteries represented with radius ∼2mm, down to a vessel radius of ∼100μm. A simulated annealing algorithm is used to identify the arterial structure that best meets the tissue's requirements. The ability to use computers to determine realistic arterial trees for organs has potential applications for computational modeling of cerebral haemodynamics, improved image segmentation, and the design of artificial organs or artificial tissue.

There are a number of popular schemes for *in-silico* arterial growth that we briefly discuss here. Early approaches for *in-silico* vascular growth used stochastic methods based on morphological data [8, 9]. A number of algorithms attempt to mimic 'sprouting angiogenesis'. This works best when modelling tumor growth [10–13]. In principle, accurate modeling of biological angiogenesis in embryo development, could precisely mimic the development of adult vasculature. However, in practice such biologically inspired arterial growth algorithms can not yet be generalized to the growth of arterial trees for large organs, which tend to be more ordered than those in tumors [14].

A different approach is to assume that the configuration of vessels in adult organs has evolved to be near

* Correspondence to: Jim.Hague@open.ac.uk

optimal, and minimizes the energy required to supply blood to tissues, while still respecting the functionality of the organ. The possibility that vasculature could be optimal was suggested by Murray [15], who showed that the sizes of parent and daughter vessels in an optimal bifurcation would follow the relation $r_p^\gamma = r_{d1}^\gamma + r_{d2}^\gamma$, where γ is a bifurcation exponent, r the radius of the vessel and subscript p and d represent parent and daughter vessels, respectively. Detailed topological examination of individual bifurcations in, e.g. the cerebral vasculature, supports this relation [16]. Constrained Constructive Optimization (CCO) grows large arterial trees by repeatedly inserting bifurcations, and then performing a local optimization [17, 18]. However, CCO has limitations when applied to hollow organs, such as the heart, and often generates trees that are too symmetrical (especially for the largest arteries) [19, 20]. In CCO, large vasculature structures are energetically sub-optimal since the optimization is local and there is no cost to intersecting areas of functional tissue. This situation can be improved by combining CCO with imaging of e.g. the large cerebral arteries, leading to impressive results [21], however, there is no single algorithm based on CCO that can handle all length scales in arterial trees on the same footing.

To address some of the well-known issues associated with CCO methods, we recently proposed a novel Simulated Annealing Vascular Optimization algorithm (SAVO) based on simulated annealing. Advantages of this algorithm are the potential to access the global minimum of total metabolic demand, the ease with which constraints can be applied during the simulation of e.g. hollow organs, and the ability to treat all length scales using identical optimization principles. We previously showed that this method could be used to generate an extensive (>6000 branch), globally optimized arterial tree, capable of supplying a hollow organ (the heart) [22]. Our approach successfully re-produced porcine cardiac morphological data.

We make special note of the approach by Kaimovitz *et al.* [23, 24], who developed a hybrid approach making heavy use of morphological data to grow very large trees featuring both arteries and veins. The trees grown using their method are impressively large, but their method is difficult to generalize. On initialization, the branching structure of their trees is selected randomly to follow morphological constraints, but from that point on, the tree topology is fixed. The treatment of different Strahler orders varies according to an *ad-hoc* scheme. They use simulated annealing to optimize the orientations of the epicardial part of this structure subject to constraints, but not to optimize the topology. The major differences with our algorithm are that (1) we have simulated annealing updates (swap node updates) that are able to explore the full configuration space of the topology of the tree, rather than setting up the tree structure on initialization (2) all levels in the tree are treated with the same universal set of principles (3) we do not require experimental data as an input to our algorithm, with the exception of the tissue shape, so any agreement with morphological data is a direct result of the algorithm and is not caused by the introduction of experimental morphological data into the algorithm.

Modeling the vascular structure of the brain presents new challenges. Unlike the heart, which can be modeled as comprising of only myocardial tissue, the brain is composed of gray and white matter with very different metabolic demand. These two tissue types have differing volumetric blood flow requirements per mass of tissue[5], which must be extracted and factored into the arterial tree generation algorithm. To the best of our knowledge, algorithms for arterial growth capable of global optimization have not been applied to the vasculature of the brain.

This paper is organized as follows. In section II the algorithm is described, and details of the segmentation of brain MR data into gray and white matter are provided. In section III, the resulting arterial trees are presented and subjected to comparisons with existing morphological *in vivo* data [25, 26]. A summary and outlook are presented in section IV.

II. MODEL AND METHODS

In this section, we detail the algorithm used to grow cerebral arterial trees *in-silico*. The primary features of the algorithm are similar to the approach used to grow cardiac vasculature [22], however, there are some differences regarding the use of MRI data to provide tissue information, and other subtleties relating specifically to the supply of cerebral tissue. We include greater detail regarding the update schemes than in our previous paper.

A. Simulated Annealing

Simulated annealing (SA) is a general optimization technique inspired by the physical process of annealing, where materials are cooled slowly to induce a higher degree of order [27]. During SA, a sequence of random modifications, or updates, are made to construct trial solutions. The probability of accepting a modification is given by the expression,

$$P_{ij} = \min\left\{\exp(\frac{-\Delta C_{ij}}{T}), 1\right\} \tag{1}$$

where P_{ij} and $\Delta C_{ij} = C_j - C_i$ are the probability and change in cost associated with altering tree configuration i to configuration j respectively. T is the annealing temperature, which is slowly reduced. The specific form of the cost function, C_i, will be discussed later. P_{ij} allows occasional acceptance of modifications that increase the cost, thus allowing the algorithm to climb out of local minima.

The annealing temperature reduction must occur slowly enough to explore the configuration space at any

given temperature. The initial, T_{init} and final T_{final} temperatures of the algorithm are chosen so that T_{init} is much larger and T_{final} much lower than the cost change associated with a typical update. The temperature schedule used here is:

$$T_{n+1} = \alpha T_n \tag{2}$$

where n denotes the simulated annealing step and the temperature multiplication factor $\alpha < 1$ is calculated via,

$$\alpha = e^{\frac{1}{S}(\ln T_{\text{init}} - \ln T_{\text{final}})}. \tag{3}$$

where S is the total number of simulated annealing steps.

We note that other optimization algorithms are available, such as genetic algorithms, ant colony, and particle swarm optimization [28–34]. The advantage of SA is its simplicity. Once the cost function has been defined and a set of ergodic updates identified, the optimization procedure is relatively straightforward, and given sufficient computational time, identification of the global minimum is guaranteed. With SA it is possible to add extra boundary constraints and cost function terms without having to modify the optimization procedure.

B. Arterial tree updates

Arterial trees are represented as a bifurcating tree. The root node is the start of the arterial tree, and represents the largest artery. The tree branches at bifurcation nodes. The simulated tree is truncated with N_{end} terminal nodes, which represent the smallest vessels we can model. Each bifurcation and terminal node of the tree has a specific 3D coordinate. Bifurcations are connected via straight vessels. Due to computational constraints, the terminal nodes are typically larger than the arterioles directly feeding the capillaries in living organisms.

Our scheme involves (1) swapping some of these connections, or, (2) moving the location of a node. One of these updates is performed at each SA step. This is the minimal set of updates that guarantees ergodicity (i.e. the algorithm can explore any tree configuration). For the spatial translation of a single bifurcation:

1. Randomly choose a bifurcation from the tree.

2. For each spatial dimension generate a uniform random number between $-d_{\text{move}}$ and d_{move}, where d_{move} is the maximum displacement distance.

3. Add the displacement to the randomly chosen bifurcation.

In practice, the tree optimizes more quickly using two different values of d_{move}.

For the node swapping (topological) update:

1. Randomly choose a node from the tree.

2. Randomly choose another node from the tree. If either randomly chosen node is upstream of the other, a new pair of nodes is selected randomly until a valid pair is found

3. Swap the parents of each node, so that the original parent of one becomes the new parent of the other, and vice versa.

TABLE I. All weightings, parameters, and target nodes for the tree modification updates in the simulated annealing algorithm. The update is chosen according to the relative weights. N.B. Updates do not apply to the root node, which is fixed.

Type	Parameter	Target	Weight
Move	$d_{\text{move}} = 1$mm	bifurcation	0.675
	$d_{\text{move}} = 1$cm	bifurcation	0.075
	$d_{\text{move}} = 1$mm	terminal node	0.045
	$d_{\text{move}} = 1$cm	terminal node	0.005
Swap	none	any node	0.2

The updates are summarized in table I.

C. Tissue voxel map and MRI data

In an improvement to our previous algorithm [22], MRI data are used to provide realistic tissue compartment shapes. To create a realistic voxel map in which to grow the cerebral arterial trees, both a T_1-weighted image and time-of-flight (TOF) angiogram from a healthy individual were collected using a 3 Tesla Siemens Skyra MR scanner (Siemens Medical, Erlangen, Germany). Spatial resolution for the two images was $1 \times 1 \times 1$ mm^3 and $0.5 \times 0.5 \times 0.5$ mm^3, respectively. The images were exported for processing in DICOM format. The angiogram was used to locate the root positions of the MCA, ACA and PCA. The T_1-weighted image was segmented into white and gray matter using the statistical parametric mapping (SPM) function in MATLAB [35]. Prior to calculation, MRI images were downscaled to reduce computational time. The surfaces of the combined white and gray matter were identified via a nearest neighbor search, where voxels having at least one unoccupied neighbor were labelled as belonging to the outer surface of the brain. A distance map from the surface voxels to all occupied voxels [36] was computed using the outline of the MRI data: Each voxel in the excluded space is assigned a value equal to the shortest distance to the surface of that space. A sample slice at each stage of the segmentation process is shown in Fig. 1. Following segmentation, we divide the brain into left and right hemispheres and perform SAVO for a single hemisphere.

Since MCA, PCA and ACA inputs are very closely spaced, a single arterial inlet representing the approximate position of these arteries as they branch from the

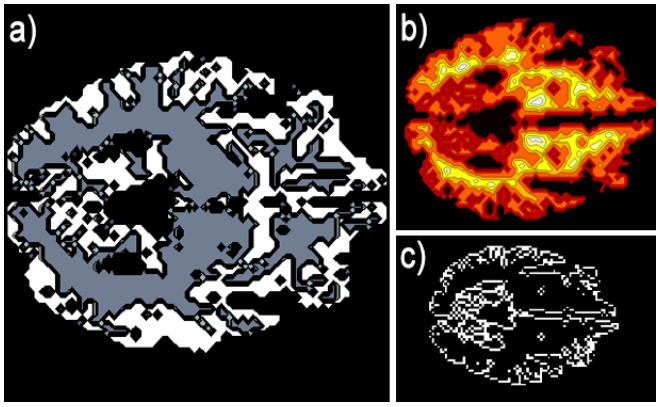

FIG. 1. An image slice of the MRI data from a healthy individual, at various stages of analysis. Panel a) shows the segmented brain tissue. b) shows the result of the distance function calculation of the brain surface, where the intensity of each voxel represents its distance to the nearest surface voxel. c) Shows the identified surface voxels of the brain.

Circle of Willis is provided to the SAVO algorithm. Relative flows are then calculated by the optimization algorithm. We are currently unable to grow arterial trees with anastamoses such as the Circle of Willis, noting that anastomoses make up a tiny proportion of vessels in arterial trees.

D. Cost Function

We define a total cost which is a measure of the fitness of a given tree,

$$C_T = A_{w,v}(C_w + C_v) + A_o C_o + A_s C_s \tag{4}$$

where $A_{w,v}, A_o$ and A_s are dimensionless constants indicating a weighting value which scales each contribution to the cost function. C_v is a metabolic cost for maintaining blood volume and C_w is the cost of pumping through a vessel; the two costs traditionally used to determine Murray's law. In addition, C_s is the penalty for over- or under-supplying tissue and C_o is a penalty associated with vessels that penetrate tissue. To form physiological trees, the blood supply cost, A_s, is given a high weight since tissue without supply would die. A high (but slightly lower) value of A_o heavily penalizes vessels that cut through parenchyma to affect organ function. Therefore A_s and A_o act as constraints.

1. Pumping cost

Following Murray [15], we assume Poiseuille flow to calculate the power dissipated during flow through a vessel, W_i,

$$W_i = \frac{8\mu l_i Q_i^2}{\pi r_i^4} \tag{5}$$

where the volumetric flow rate is f, the vessel is assumed cylindrical with radius r and length l and we use a representative and constant value for the viscosity of blood $\mu = 3.6 \times 10^{-3}$Pa s (although we note that blood viscosity can drop significantly in small vessels $< 100\mu$m [37]). By calculating flow in each artery of the tree the total power dissipation, $C_w = \sum_i W_i$ can be estimated.

For computational efficiency, we maintain a constant input flow, and terminal flows are also assumed to be fixed and equal. Thus, from conservation of mass, the flow in any artery depends only on the number of terminal sites downstream. If f_{root} represents the total flow into the tree, the total flow per end node is $f_{\text{term}} = f_{\text{root}}/N_{\text{end}}$. A power law is used to relate radii and flow in various tissue types [38], $f = \epsilon r^\gamma$, where γ is the bifurcation exponent which is set in advance of the simulation from experimental considerations and ϵ is a constant determined from the flow and radius of the root artery. This reduces the computational complexity significantly.

2. Metabolic cost for maintenance of blood volume

Following Murray [15], we assume that there is a cost to maintain a volume of blood:

$$C_v = m_b \sum_i V_i. \tag{6}$$

We have used a value of $m_b = 648\text{J s}^{-1}\text{ m}^{-3}$, which is within the measured range for humans [39] and V_i is the total volume of a cylindrical arterial segment.

3. Blood Supply Penalty

In a healthy organism, on average (over a physiologically long timescale) perfusion is even throughout tissue [40]. Thus, terminal nodes should be positioned such that the supply is uniform. The terminal nodes in SAVO are much larger than capillaries, so we consider terminal nodes to be surrounded by microcirculatory "black boxes" [17] with a sphere of influence of radius R_{supply}. Within each sphere the details of the microvasculature are neglected. Without this assumption the computational power required to optimise the tree would be prohibitive. The radius of the spheres is calculated using physiological values for the blood demand of the tissue under consideration as,

$$4\pi R_{\text{supply}}^3/3 = f_{\text{term}}/q_{\text{req}}, \tag{7}$$

where q_{req} is the volumetric blood flow required to maintain tissue. Gray and white matter in the brain have different supply requirements [5], $q_{\text{req,gray}} = 10.9 \times 10^{-3}\text{s}^{-1}$ and $q_{\text{req,white}} = 3.57 \times 10^{-3}\text{s}^{-1}$ respectively, leading to a smaller R_{supply} and thus higher density of terminal nodes sited in the gray matter following Eq. 7. [41]. The total flow is determined using q_{req} and the total volume

of gray and white matter in the MRI scans, which are $389.12 \times 10^{-6}\mathrm{m}^3$ and $321.64 \times 10^{-6}\mathrm{m}^3$ respectively.

There is no unique way to define the supply penalty. We select it to be,

$$C_s = \sum_{\mathbf{voxels}} s;\ s = \begin{cases} 10 & \text{if } b = 0 \\ (b-1)^2 & \text{otherwise} \end{cases} \tag{8}$$

where b is the total number of spheres contributing to the supply of a single voxel in the tissue and the sum is performed over all the voxels comprising the tissue. C_s favors voxels supplied by a single sphere, and thus encourages spheres to pack the tissue as densely as possible while minimizing overlap. We note that this cost only needs to be calculated if a terminal node moves.

4. Exclusion of Large Arteries

Larger arteries are absent from regions of many organs as they would interfere with function. For example the brain has large arteries (the pial arteries) running across its surface, whereas only the smaller arteries branching from the pial arteries are allowed to penetrate. Also, gray matter has approximately double the blood supply requirements of white matter[4], which may play a role in bringing the larger arteries to the surface.

A distance map is used to calculate a penalty that increases the deeper a vessel lies within the excluded tissue, to enforce exclusion of larger vessels. We define a cutoff radius R_{ex} whereby any node exceeding this radius incurs a cost,

$$C_o = \sum_{\mathrm{nodes}} D_{ijk}^3, \tag{9}$$

where i, j and k are voxel coordinates and D_{ijk} is the distance map value. We note that this is a slightly different penalty than used previously, but is much faster to compute than the Bresentham based algorithm we described before.

Cerebral arterioles with diameters less than $\sim 100\mu m$ are responsible for penetrating deep within cortical tissue[42]. For even our largest trees the smallest vessels are slightly wider than this value. We select R_{ex} in the range 100μm to 150μm to ensure some penetration into the tissue, and to understand how results are modified by changes in R_{ex}.

E. Outline of the algorithm

We now summarize the whole SAVO algorithm. The initialization steps are as follows:

1. Generate a maximally asymmetric tree with N terminal nodes by (a) connecting the root node to a terminal node (b) introducing a connection node between the terminal node and its parent, and attaching another terminal node to this connection (c) repeating steps (a) and (b) $N-1$ times.
2. Assign the position of each non-terminal node of the tree to a random location in space.
3. Assign each terminal node a random position inside the tissue area to be perfused.
4. Randomize the topology of the tree by repeatedly applying the swap node move $1000 \times N$ times.
5. Traverse through the tree from a terminal node to the root, add f_{term} to the flow of each node visited. Repeat for all terminal nodes.
6. For each node, calculate its radius $(f/\epsilon)^{1/\gamma}$.
7. Calculate the initial value of the cost function using Eq. 4.

Once initialized, the tree is in a random but valid topological and spatial state. The optimization procedure is as follows:

1. Randomly choose and apply an update using the weightings found in table I.
2. Calculate the cost function using Eq. 4 for the newly modified tree.
3. Using the simulated annealing condition of Eq. 1, accept or reject the modification. If rejected, revert the tree to its previous state.
4. If the trial vasculature has the lowest value of the cost function yet achieved, then record the tree state.
5. Reduce the simulated annealing temperature according to Eq. 2.
6. Repeat the previous steps S times.

A full list of parameters used in the SAVO algorithm is provided in table II. If multiple trees are simulated with the same input parameters, then we analyze the one with the lowest overall value of the cost function.

For large trees, the total number of topological states is vast, and good optimization can only be achieved for very large numbers of simulated annealing steps. Every effort was made to ensure the code was optimized. For the swap node move, caching the modified nodes saved time whenever the move was rejected, as they did not have to be recalculated and the probability of rejection of that move is high, especially towards the end of optimization. The algorithm was implemented in C++ making full use of the 2011 standard library, and was compiled with the O3 flag for maximum optimization. Subsequent data analysis of the generated trees was performed using a mix of python, MATLAB and C++. The optimization of an 8191 node tree in a realistic geometry takes a few

TABLE II. Input parameter names, symbols, values and typical sources.

Parameter	Symbol	Value	Source
Flow requirement (gray)	$q_{\mathrm{rec,gray}}$	10.9×10^{-3} (m^3 / s) / m^3 brain	SPECT
Flow requirement (white)	$q_{\mathrm{rec,white}}$	3.57×10^{-3} (m^3 / s) / m^3 brain	SPECT
Volume (gray)	V_{gray}	389.12×10^{-6} m^3	MRI
Volume (white)	V_{white}	321.64×10^{-6} m^3	MRI
Root flow	$q_{\mathrm{rec,gray}}V_{\mathrm{gray}} + q_{\mathrm{rec,white}}V_{\mathrm{white}}$	323.4 ml / min	Calculated
Root radius	r_{root}	1.5 mm	Based on physiology
Root position	N/A	Average of MCA, PCA, ACA	TOF MRI
Branching exponent	γ	3.2	MRI
Metabolic constant	m_b	648 J $s^{-1}m^{-3}$	PET
Node exclusion parameter	R_{ex}	100μm / 150μm	Based on physiology
No. nodes	N	8191 / 16383	Selected
No. end nodes	N_{end}	4096 / 8192	Selected
SA steps	S	10^{10}	Selected
SA initial temperature	T_{init}	10^{12}	Selected
SA final temperature	T_{final}	10^{-10}	Selected
Cost function weight	$A_{w,v}$	1×10^4	Selected
Exclusion penalty	A_o	1×10^{15}	Selected
Supply penalty	A_s	1×10^{30}	Selected

days on an Intel i7 2.8GHZ desktop PC. This timescale grows rapidly with tree size (we used the Open University IMPACT cluster to carry out multiple calculations with different random number seed and larger tree sizes). We make several anneal runs for each parameter set with different random number generator seed. For the displayed data the variance on the final cost function from these runs was small, indicating convergence of the algorithm on optimal solution.

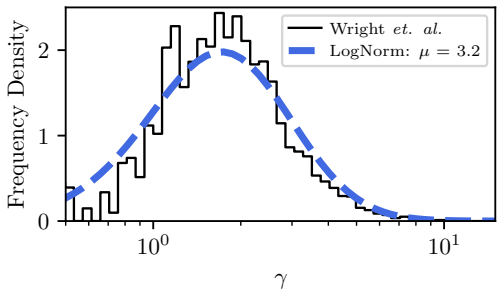

FIG. 2. Histogram showing the distribution of γ values in the MRI data of Wright *et al.* [25, 26]. Fit of a log normal curve to the histogram indicates a mean value of 3.2 for γ.

F. Comparison data

Comparison trees were taken from the BraVa database [25, 26]. Wright *et. al.* extracted cerebral arterial tree morphometry from 3T time-of-flight MRA high-resolution images of 61 healthy volunteers, and then segmented the trees manually from MRI image slices using the ImageJ software package. We have reanalyzed the data so that there is only a single root point, consistent with our generation algorithm, and to use diameter defined Strahler order (DDSO) which leads to better classification of vessel segments [43]. We performed our morphological analysis on the trees using Python. Trees were discarded from the dataset if they had any arteries labeled as zero radius (BG06, BH0040, BI0001, Set10, Set8, Set9) or if the DDSO algorithm failed to converge (BG0020, BH0009, BH0026).

Sensitivity analysis for 2D trees found in the appendix indicates that the tree structure is only sensitive to the bifurcation exponent, γ. Bifurcations in the data were analyzed to estimate the bifurcation exponent. Results are shown in Fig. 2. We have performed a separate analysis of bifurcations in the BraVa database, which found the mean to be $\gamma = 3.2$. We use $\gamma = 3.2$ throughout.

III. RESULTS OF ARTERIAL TREE GROWTH

Figure 3 shows the appearance of the vasculature generated for a single hemisphere with $N = 8181$ (panel (a)), $N = 16383$ (panel(b)) and an MRI vasculature captured by Wright et al. [25, 26] (panel (c)). $R_{\rm ex} = 150\mu$m. The smallest vessels that can be made out in the MRI vasculature have a radius of approximately 0.31mm due to the limited resolution of the imaging technique. There are several similarities between the vascular trees. Large sections of the arteries run across the outer surface of the brain, mimicking the pial arteries. We note that this feature of the structure improves with the number of vessel segments. While the computed arterial trees lack tortuosity, similar forms of the major arteries are seen.

The first panel of Figure 4 shows the mean arterial radius, r, vs diameter defined Strahler order (DDSO). MRI data were averaged over all trees, whereas the computational data is averaged over only the tree with lowest cost. Error bars show a standard deviation of the data (note that we are interested in the spread of the data, rather than the standard error on the mean). For the radius, general agreement with experimental data is good. The leveling out of the radius seen in the MRI data for smaller Strahler orders may be related to overestimation of the smallest radii in the MRI data due to resolution effects. We also show histograms of radii, $N(r)$ sorted by diameter-defined Strahler order (Figure 4, remaining panels). In these plots, we also include data from a single MRI measured tree (BG001). The overall behavior of the radii as a function of branching order is matched between the experimental and generated data. The histograms are approximately Gaussian distributed, and there is a similar spread, with the exception of the histogram of highest Strahler order which has a wider spread in the MRI data than the computational data.

Next, we examine the asymmetry ratios, $r_p/r_{d>}$ and $r_p/r_{d<}$, where r_p is the parent vessel radius, $r_{d>}$ and $r_{d<}$ are the radii of the larger and smaller daughter vessels in the bifurcation respectively, which are shown in Fig. 5. Branching ratios are expected to tend to $1/2^{1/\gamma}$ (approximately 0.8 for $\gamma = 3.2$) since arterial trees must necessarily become more symmetric as they become smaller. This can be understood by considering the final arterioles before the capillary bed, which are of roughly equal size, so the final bifurcation before the capillary bed must be roughly symmetric. An oddity of the BraVa MRI data [25, 26] is that the branching ratio of the largest branch is bigger than 1 for lowest Strahler order, which is surprising because it indicates that some vessels get wider after branching (rather than smaller as is normally the case). We have thoroughly checked that this effect is present and believe that this occurs due to an effective discretization of the MRI data due to the 0.31mm voxel resolution. In order to get a more meaningful comparison of the generated trees to the BraVa database [25, 26] the effects of MRI resolution are replicated in the computational trees. The effect of the MRI and subsequent

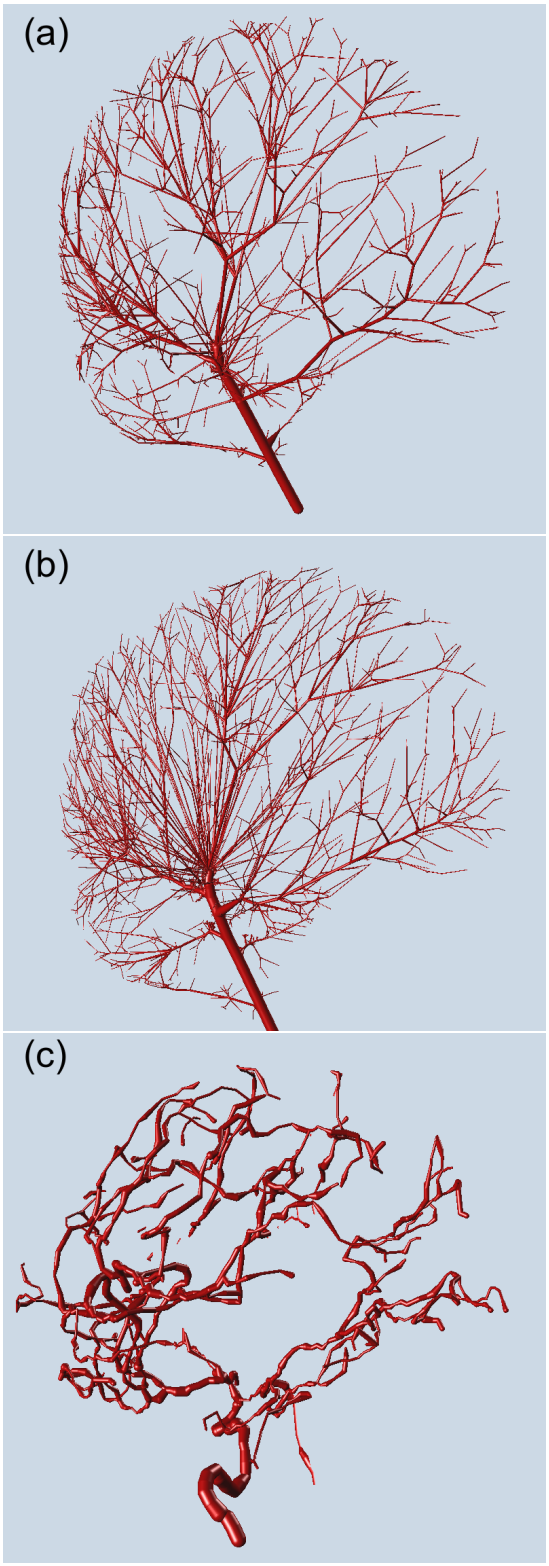

FIG. 3. (a) Cerebral vasculature automatically generated on a geometry obtained from MRI imaging (8191 seg.). (b) Cerebral vasculature automatically generated on a geometry obtained from MRI imaging (16383 seg.) (c) Single hemisphere of MRI vasculature from the BraVa database (patient BG001) [25, 26]. All images are rendered using VAA3D [44–46].

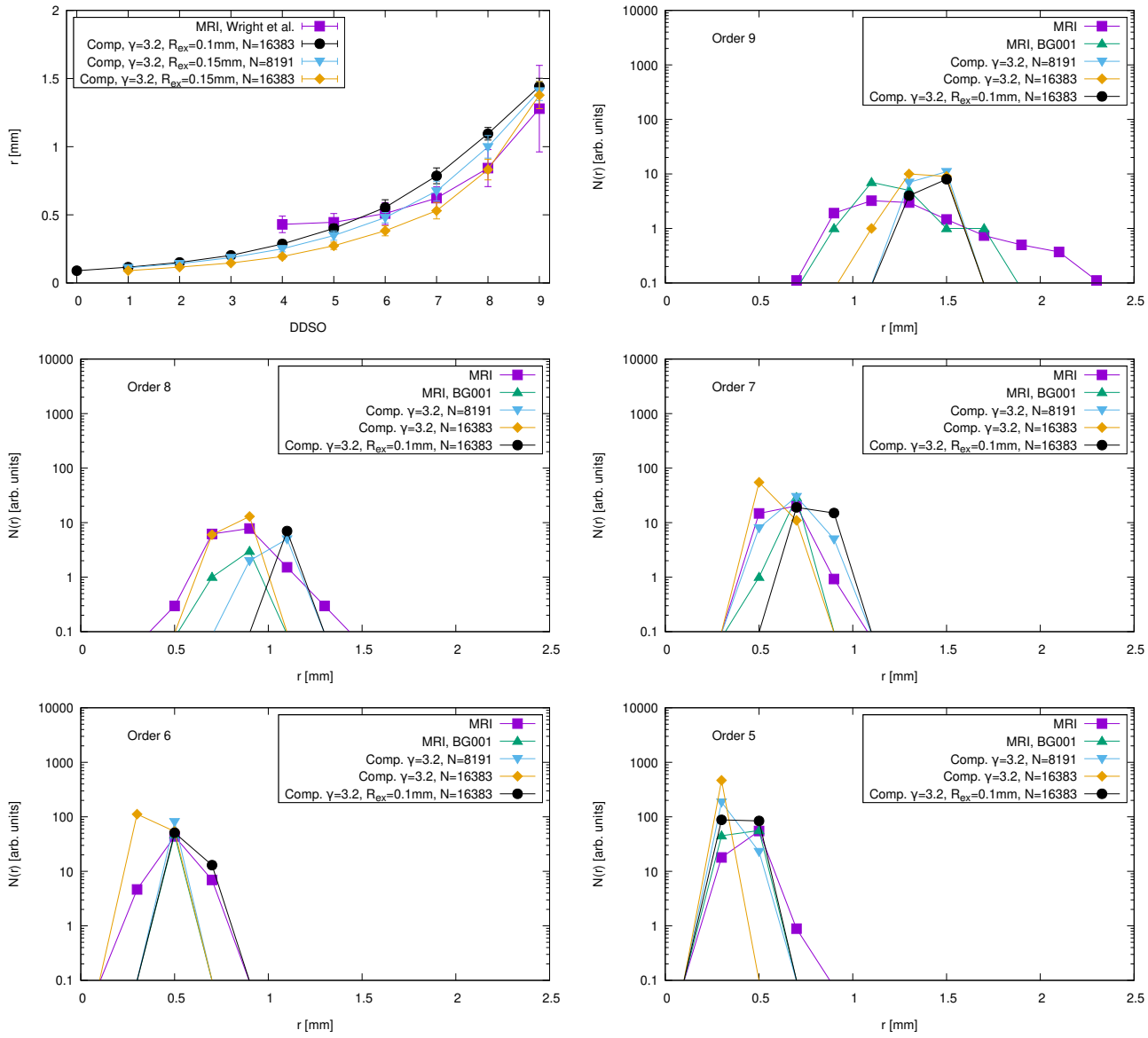

FIG. 4. Plot showing the mean radii of the generated tree vs the experimental data of Wright et. al. [25, 26] as a function of Strahler order. Bars show a standard deviation.

segmentation is to prune small arteries from the tree and discretize the radius, which is relatively straightforward to replicate in the generated trees by including only the arteries with radius greater than a cutoff, $R_C \geq 0.28$mm, and discretizing the radius in steps of R_C above this value by rouding down to the nearest multiple of R_C (this discretizaton originates from voxelization and is seen in the BraVa data). For around 20% of the radii, we also add an additional voxel width at random to emulate aliasing effects for vessels that sit close to voxel boundaries and therefore appear to be wider than their true width by an extra voxel. We chose R_C so that it is as close as possible to the MRI resolution cutoff, while maintaining the same number of Strahler orders as the MRI data. While crude, the pruning process gives the computational data a form close to the MRI data, with both curves lying within the variance of the MRI data.

Finally in Fig. 6 we examine the relationship between length and branching order for the generated tree. The first panel of Fig. 6 shows the mean lengths of the vessels vs Strahler order. We have included the mean for the whole MRI data set, the mean for a single MRI tree (BG001), and computationally generated trees for different values of N and $R_{\rm ex}$. A pruned tree with $N = 16383$ and $R_{\rm ex} = 0.1$mm is also shown. For length measurements, the pruning procedure is very important, since the effect of finite MRI resolution is an apparent lack of small branches from major vessels in the MRI data, potentially leading to overestimation of segment length. On the other hand, the computational data have only

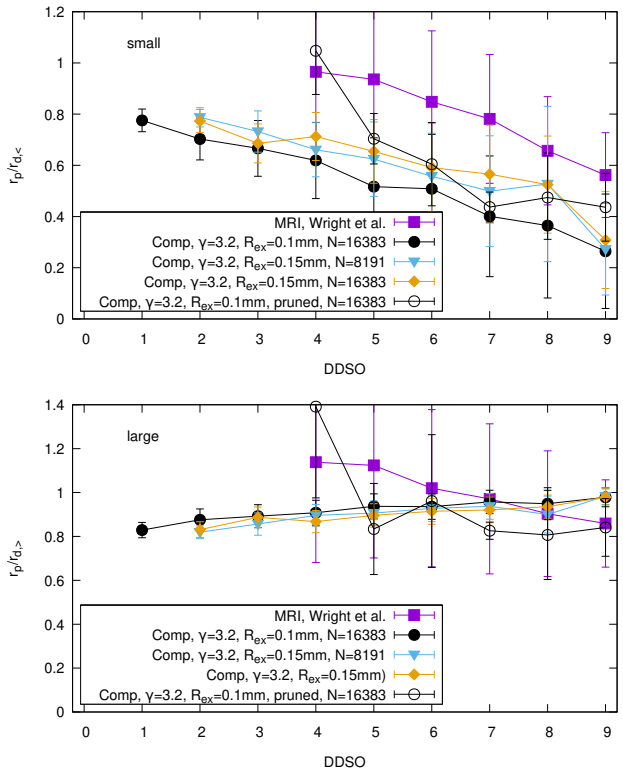

FIG. 5. Plot showing the asymmetry ratios, $r_p/r_{d>}$ and $r_p/r_{d<}$, vs Strahler ordered for MRI and *in-silico* data. Bars show a standard deviation.

short lengths between bifurcations due to large numbers of small vessels branching from major arteries that would not be imaged by MRI, and thus obscure the comparison. Examining the pruned data, the mean lengths of the largest Strahler order are roughly consistent between measured and *in-silico* trees. Lengths of vessels in the MRI data appear to increase slightly as radius decreases, whereas the pruned computational data decreases in length before increasing at lower Strahler order. Changing the number of vessels in the computational tree does not lead to any significant changes in the unpruned lengths. However, changes in R_{ex} do lead to a small increases in length at the highest Strahler order, presumably because the vessels have to follow the surface of the brain over a longer distance before penetrating the tissue. Ideally, we would grow trees using the physiological value of $R_{\text{ex}} = 50\mu$m. We estimate that meaningful examination of trees with $R_{\text{ex}} = 50\mu$m would require trees with the order of 100000 segments, so that the smallest vessel radius is less than R_{ex}. This is outside our current computational capability.

Other origins for the differences in mean lengths can be seen by examining histograms showing the distribution of lengths by diameter-defined Strahler order found in the remaining panels of Fig. 6. Lengths are non-Gaussian distributed and follow a power law distribution for larger l. The computational trees have more short vessels at all orders. This could be due to under-representation of short vessels in the MRI data due to e.g. resolution effects or an over-representation of short vessels in the computational data. The histograms also show that more long vessels are present in the MRI data.

IV. DISCUSSION AND CONCLUSIONS

In this article, we have applied a simulated annealing based method to *in-silico* growth of the arterial trees supplying the brain. Our SAVO algorithm is capable of approaching the global cost minimum, handling complex organ shapes and excluding large vessels from tissue. This contrasts with CCO, which needs to be adapted for each situation and struggles to reproduce the vasculatures of complex organ shapes. It also contrasts to morphologically based arterial growth algorithms, which require detailed experimental data to run, making application to new organs difficult.

Morphological analysis shows that the radii and asymmetry ratios of vessels in the human brain are well represented by the optimized trees. The lengths of vessels are shorter than found in MRI data, and sensitive to the exclusion radius, R_{ex}, which is approximately double the physiological value in our algorithm. Agreement improves as the exclusion radius is made smaller, although further reduction of this value requires the number of nodes in our algorithm to be increased significantly (we are not currently able to generate larger trees due to computational constraints). Agreement in lengths improves significantly once the pruning effects of MRI resolution are taken into account. The visual structure of the generated trees compares well with the form of the major arteries measured using MRI, especially the pial arteries that traverse the surface of the brain, although with the caveat that the arterial trees grown with the algorithm are straight and lack tortuosity. The agreement of the radii indicates that the trees could be used in models of embolic stroke and cerebral autoregulation (see [47–50]). This will form part of a future paper.

Overall, the algorithm has significant potential. It has been shown to be capable of growing vascular trees for two large organs with complex vasculature (the heart and brain). Our *in-silico* models match morphological data, and reproduce features that would be difficult, if not impossible, to reproduce with CCO, without the need for detailed measurements of morphological data. Further extensions should demonstrate the possibility of growing arterial and venous vascular structures simultaneously. Greater efficiency would allow the growth of much larger trees (including multiscale growth), and the possibility of describing tortuous vessels by introducing kink nodes without bifurcations to the algorithm.

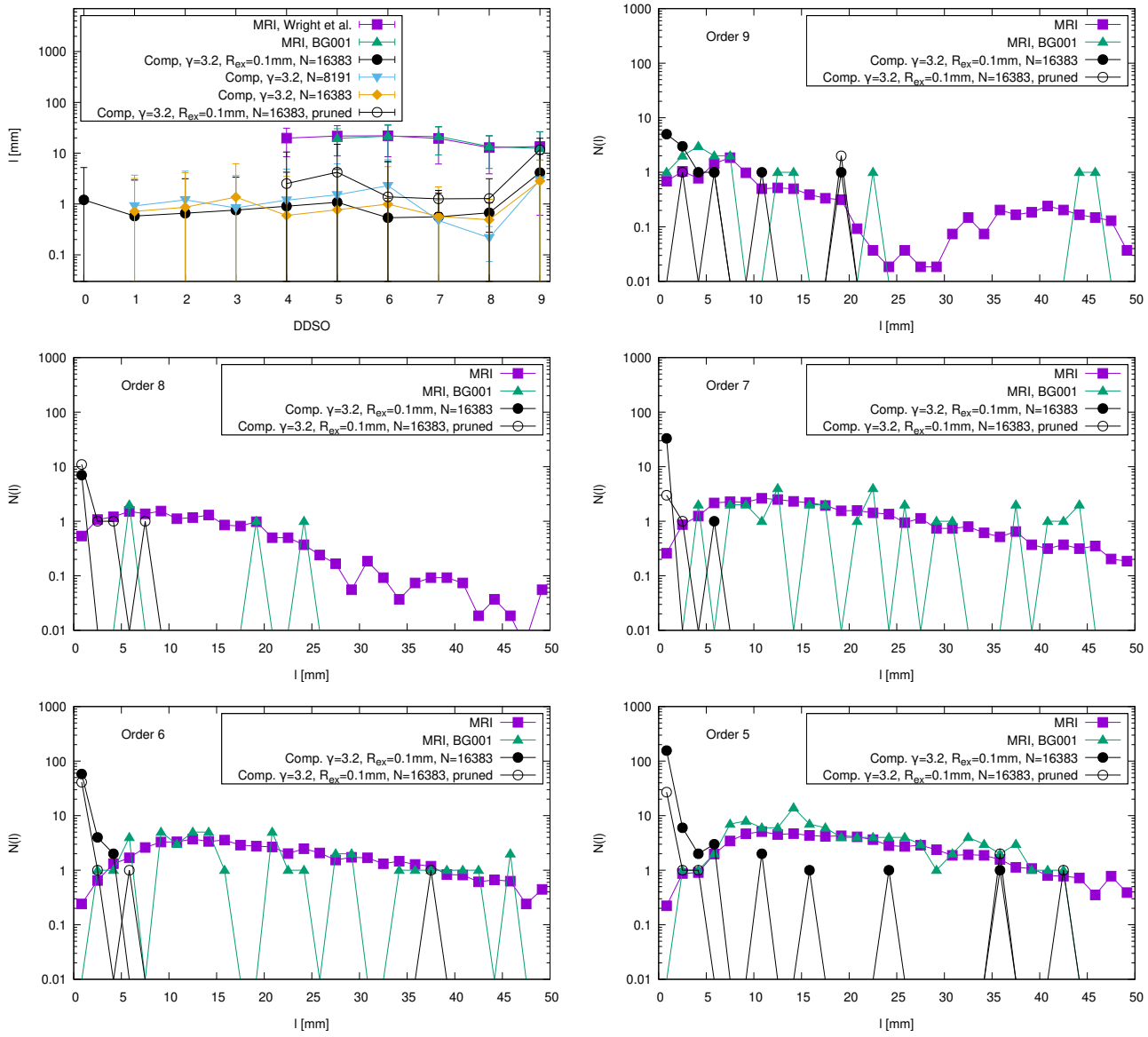

FIG. 6. Plot showing the mean lengths of various branches of the generated tree vs the experimental BraVa data [25, 26] as a function of branching order (top left). Bars show a standard deviation. Histograms comparing the length distributions in MRI and computational data at various Strahler orders are also shown.

ACKNOWLEDGEMENTS

JK acknowledges support from EPSRC grant EP/P505046/1. EC acknowledges support from EPSRC grant number EP/L025884/1. We declare we have no competing interests. We would also like to thank Mark Horsfield (Xinapse systems) for help with the MRI scans.

AUTHORS' CONTRIBUTIONS

JK developed the algorithm and analysis code, acquired, analysed and interpreted data. EC managed MRI data and co-supervised the project. JPH conceived the study, developed initial versions of the algorithm, acquired, analysed and interpreted data, and supervised the project. All authors contributed to drafting the article and gave final approval for publication.

[1] S. J. Payne. *Cerebral Blood Flow and Metabolism: A Quantitative Approach.*

[2] P. Hartmann, A.Ramseier, F.Gudat, M.J.Mihatsch, and W.Polasek. *Der Pathologe*, 15:165–170, 1994.

[3] S.S.Kety and C.F.Schmidt. *J Clin Invest.*, 27:484–492, 1948.

[4] Richard SJ Frackowiak, Gian-Luigi Lenzi, Terry Jones, and Jon D Heather. *Journal of computer assisted tomography*, 4(6):727–736, 1980.

[5] Peiying Liu, Jinsoo Uh, Michael D. Devous, Bryon Adinoff, and Hanzhang Lu. *NMR in Biomedicine*, 25(5):779–786, 2012.

[6] Sylvie Lorthois, Francis Cassot, and Frederic Lauwers. *Neuroimage*, 54(4):2840–2853, 2011.

[7] N.J.Abbott, A.A.Patabendige, D.E.Dolman, S.R.Yusof, and D.J.Begley. *Neurobiol Dis.*, 37:13–25, 2010.

[8] C. Wang, J. B. Bassigthwaighte, and L. J. Weissman. *Math. Comput. Model.*, 16:91–98, 1992.

[9] H. Qian and J. B. Bassingthwaighte. *J. Theor. Biol.*, 205:261–268, 2000.

[10] Holger Perfahl, Helen M. Byrne, Tingan Chen, Veronica Estrella, Toms Alarcn, Alexei Lapin, Robert A. Gatenby, Robert J. Gillies, Mark C. Lloyd, Philip K. Maini, Matthias Reuss, and Markus R. Owen. *PLoS ONE*, 6(4):e14790, 04 2011.

[11] A.R.A. Anderson and M.A.J. Chaplain. *Bulletin of Mathematical Biology*, 60(5):857–899, 1998.

[12] Steven R. McDougall, Alexander R.A. Anderson, and Mark A.J. Chaplain. *Journal of Theoretical Biology*, 241(3):564 – 589, 2006.

[13] Anusuya Das, Douglas Lauffenburger, Harry Asada, and Roger D. Kamm. *Philosophical Transactions of the Royal Society of London A: Mathematical, Physical and Engineering Sciences*, 368(1921):2937–2960, 2010.

[14] J.A. Nagy, S-H Chang, A.M.Dvorak, and H.F.Dvorak. *British Journal of Cancer*, 100:865–869, 2009.

[15] C.D. Murray. *Proceedings of the National Academy of Sciences of the United States of America*, 12(3):207, 1926.

[16] S.Rossitti and J.Lfgren. *Stroke*, 24:371–377, 1993.

[17] W Schreiner and P F Buxbaum. *IEEE transactions on bio-medical engineering*, 40(5):482–91, May 1993.

[18] R Karch, F Neumann, M Neumann, and W Schreiner. *Annals of Biomedical Engineering*, 28(5):495–511, May 2000.

[19] W Schreiner, F Neumann, M Neumann, R Karch, A End, and S M Roedler. *The Journal of general physiology*, 109(2):129–140, 1997.

[20] Wolfgang Schreiner, Rudolf Karch, Martin Neumann, Friederike Neumann, Paul Szawlowski, and Susanne Roedler. *Medical Engineering & Physics*, 28(5):416–429, 2006.

[21] A.A. Linninger et al. *Ann Biomed Eng*, 41:2264, 2013.

[22] J. Keelan, E.M.L. Chung, and J.P. Hague. *R. Soc. Open. Sci.*, 3:150431, 2016.

[23] Benjamin Kaimovitz, Yoram Lanir, and Ghassan S Kassab. *Annals of biomedical engineering*, 33(11):1517–35, November 2005.

[24] B Kaimovitz, Y Lanir, G S Kassab, S Nees, G Juchem, N Eberhorn, M Thallmair, S Förch, M Knott, A Senftl, T Fischlein, B Reichart, D R Weiss, and H G M Van Beek. *Am J. Phys. Heart Circ. Phys.*, 299(July 2010):1064–1067, 2010.

[25] Susan N. Wright, Peter Kochunov, Fernando Mut, Maurizio Bergamino, Kerry M. Brown, John C. Mazziotta, Arthur W. Toga, Juan R. Cebral, and Giorgio A. Ascoli. *NeuroImage*, 82:170–181, 2013.

[26] http://cng.gmu.edu/brava.

[27] Emile Aarts, Jan Korst, and Wil Michiels. pages 187–210. Springer, 2005.

[28] Manoj Kumar, Mohammad Husian, Naveen Upreti, and Deepti Gupta. *International Journal of Information Technology and Knowledge Management*, 2(2):451–454, 2010.

[29] Christopher R Houck, Jeff Joines, and Michael G Kay. *NCSU-IE TR*, 95(09), 1995.

[30] Marco Dorigo and Christian Blum. *Theoretical computer science*, 344(2):243–278, 2005.

[31] Christian Blum. *Physics of Life reviews*, 2(4):353–373, 2005.

[32] James Kennedy. pages 760–766. Springer, 2010.

[33] Alec Banks, Jonathan Vincent, and Chukwudi Anyakoha. *Natural Computing*, 7(1):109–124, 2008.

[34] Hongnian Zang, Shujun Zhang, and Kevin Hapeshi. *Journal of Bionic Engineering*, 7:S232–S237, 2010.

[35] AR Pries, Timothy W Secomb, P Gaehtgens, and JF Gross. *Circulation research*, 67(4):826–834, 1990.

[36] Heinz Breu, Joseph Gil, David Kirkpatrick, and Michael Werman. *Pattern Analysis and Machine Intelligence, IEEE Transactions on*, 17(5):529–533, 1995.

[37] R. Fahraeus and T. Lindqvist. *The American Journal of Physiology*, 96:562568, 1931.

[38] Geoffrey B West, James H Brown, and Brian J Enquist. *Science*, 276(5309):122–126, 1997.

[39] Y Liu and G S Kassab. *American journal of physiology Heart and circulatory physiology*, 292(3):H1336–H1339, 2007.

[40] I.M.S. Wilkinson, J.W.D. Bull, G.H. du Boulay, J. Marshall, R.W.Ross Russell, and L. Symon. pages 17–18. Springer Berlin Heidelberg, 1969.

[41] The quoted supply values assume a homogeneous metabolic requirement in cortical tissue, which is a simplification, however as the algorithm does not simulate cerebral function we assume that the large majority of temporal fluctuations are averaged out to some degree. We assume that a single tissue type in the brain requires, on average, a fixed amount of blood flow.

[42] Francis Cassot, Frederic Lauwers, Céline Fouard, Steffen Prohaska, and Valerie Lauwers-Cances. *Microcirculation (New York, N.Y. : 1994)*, 13(1):1–18, January 2006.

[43] Z. L. Jiang, G. S. Kassab, and Y. C. Fung. *J. Appl. Physiol.*, 76(2):882–892, Feb 1994.

[44] H. Peng et al. *Nature Biotechnology*, 28.

[45] H. Peng et al. *Nature Protocols*, 9:193–208, 2014.

[46] H. Peng et al. *Nature Communications*, 5:4342, 2014.

[47] Emma M L Chung, James P Hague, and David H Evans. *Physics in Medicine and Biology*, 52(23):7153, 2007.

[48] J. P. Hague and E. M. L. Chung. *Phys. Rev. E*, 80:051912, Nov 2009.

[49] J. P. Hague and E. M. L. Chung. *International Journal of Modern Physics B*, 23(20n21):4150–4157, 2009.

[50] J.P. Hague, C. Banahan, and E.M.L. Chung. *Phys. Med. Bio.*, 58:4581, 2013.

TABLE III. Input parameters modified for sensitivity analysis, their mean values and standard deviation

Name	symbol	Mean	σ	Units
Bifurcation Exponent	γ	3.0	1	N/A
Metabolic Constant	m_b	640	100	J $m^{-3}s^{-1}$
Root Radius	r_{root}	1	0.5	mm
Root Flow	f_{root}	10^{-5}	0.5×10^{-5}	m^3s^{-1}

Appendix A: Sensitivity Analysis

The input parameters to the algorithm are subject to both natural biological variation and measurement error. To quantify the effects that this uncertainty may have on the generated trees we undertook a sensitivity analysis of the input parameters of the arterial generation algorithm on a 2D tree. The aim was to understand to what extent variation in the input parameters can affect the morphology and structural properties of the generated trees. To achieve this we first assume that all input parameters follow a normal distribution with respect to natural variation and measurement error. In this way the probability distribution of input parameter x is characterised by its mean value $\langle x \rangle$ and its standard deviation σ_x. From this distribution sample input states can be drawn with probability weighted by the individual input parameter distributions. A single input state thus comprises a set of values for the various input parameters contained in Table III, where each value is drawn from a probability distribution describing that parameter. In the following sensitivity analysis we keep the number of nodes N fixed at 256. Since a large number of trees need to be optimized to achieve good statistics, we also limit the tree growth to a 2D plane of size 1 cm by 1 cm, with the root node placed in the center.

To perform the sensitivity analysis, random input states were generated from the probability distributions of each input parameter. A tree was then optimised from this initial state. This process was repeated 500 times to draw a representative sample from the distribution of input states.

To quantify the effect of varying the input parameters, we have examined a range of measures to examine both the network structure and the individual arterial segment geometry. The radius of an arterial segment is given by r_i, the length by l_i. The subscripts c_1 and c_2 denote the two child arteries of a bifurcation, where it is assumed in a ratio calculation that the denominator holds the larger value, so that the ratio is always less than one. Total length is defined as $\sum l_i$, the sum of all lengths of arterial segments in the tree. Path Length is $\langle \sum_{\text{path}} l_i \rangle$, representing the average summed path length from root to terminal node. Radius to length ratio is defined as, $\langle \frac{r}{l} \rangle$. Radius asymmetry as $\langle \frac{r_{c_1}}{r_{c_2}} \rangle$ measures the asymmetry the radii of the child arteries of a bifurcation ($r_{c1} \geq r_{c2}$). Length asymmetry, $\langle \frac{l_{c_1}}{l_{c_2}} \rangle$ measures asymmetry in lengths of the child arteries of a bifurcation ($l_{c1} \leq l_{c2}$).

The results of the analysis are presented in Figure 7. The figures show projections along the axis represented by the relevant input parameter, and the values of the various tree properties are scaled by the mean of the entire population of simulated trees. It can be seen that by far the most dominant factor controlling the variation in the morphological properties is the bifurcation exponent. The other input parameters had very little effect over the range of values investigated, which in some cases represented a measurement with almost 50% error. While the bifurcation exponent can produce large variations in the various morphological and structural properties of the tree, it can be seen from figure 7 that in the typical range of biological tissue (0.75 - 1.2 on the x-axis, 2.0 to 4.0), all parameters except the length asymmetry are relatively stable. There is still, however, some variation even in this region.

The results of the sensitivity analysis have shown that changes in γ produce the largest variations. In spite of this, the results show that the generated trees enter a relatively stable regime inside the region of typical biological values (2.0 - 4.0). This suggests that for $\gamma = 3.2$ (used to generate the cerebral vasculature) even a 10% error in its measurement would not affect the resultant trees to a significant extent. The other parameters are shown to have very little effect on the properties of the generated trees, even up to a 40% relative error.

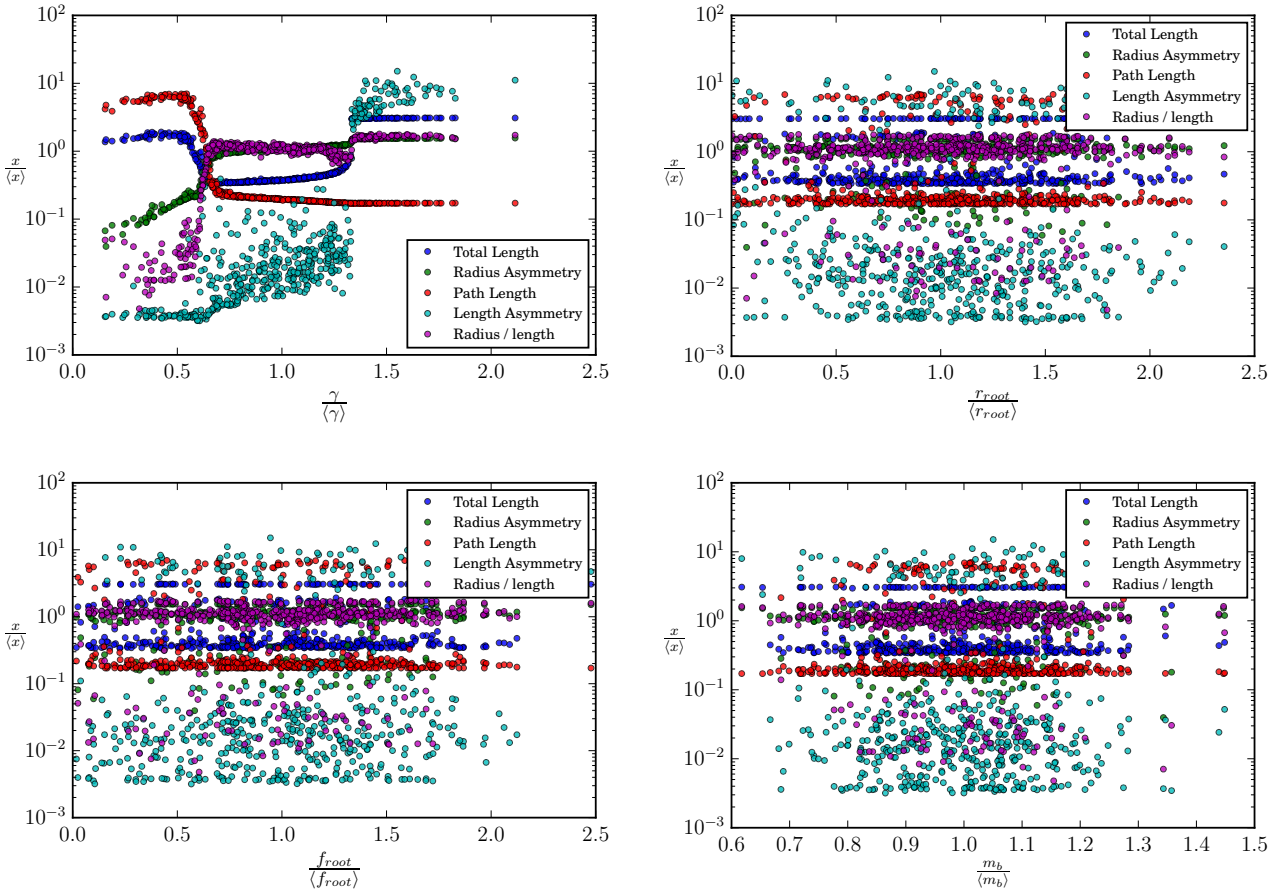

FIG. 7. (a) Variation of tree morphology with changing bifurcation exponent γ. The bifurcation exponent is the most dominant factor with regards to tree morphology. (b) Variation of tree morphology with changing root radius r_{root}. (c) Variation of tree morphology with changing root blood flow f_{root}. (d) Variation of tree morphology with changing metabolic constant m_b.